JOURNAL OF CATALYSIS **162,** 31–47 (1996)
ARTICLE NO. 0257

Characterisation of Variations in Vanadium Phosphate Catalyst Microstructure with Preparation Route

Christopher J. Kiely,* Andrew Burrows,* Sujata Sajip,* Graham J. Hutchings,† Maria Teresa Sananes,‡ Alain Tuel,‡ and Jean-Claude Volta‡

*Department of Materials Science and Engineering, University of Liverpool, P.O. Box 147, Liverpool, L69 3BX, United Kingdom; †Leverhulme Centre for Innovative Catalysis, Department of Chemistry, University of Liverpool, P.O. Box 147, Liverpool, L69 3BX, United Kingdom; and ‡Institut de Recherches sur la Catalyse, CNRS, 2 Avenue Albert Einstein, 69626, Villeurbanne Cedex, France

Received August 10, 1995; revised April 9, 1996; accepted April 11, 1996

Three vanadium phosphate catalysts prepared by different methods are compared and contrasted for the selective oxidation of *n*-butane to maleic anhydride. $VOHPO_4 \cdot 0.5H_2O$ catalyst precursors were prepared via three distinct routes: (a) using aqueous HCl as a reductant for V_2O_5, (b) using isobutanol as solvent and reductant for V_2O_5; and (c) using isobutanol as a reducing agent for $VOPO_4 \cdot 2H_2O$. The precursors were transformed under identical conditions (385°C, 1.5% butane in air, 1000 h^{-1}, 75 h) to three activated catalysts. The morphology of the precursors and the final catalysts have been assessed using a combination of X-ray diffraction (XRD), scanning electron microscopy (SEM), transmission electron microscopy (TEM), and ^{31}P NMR spin-echo mapping. Even though they exhibited very similar *specific* activities for maleic anhydride production, the three activated vanadium phosphate catalysts were found to have widely varying morphologies. The implications of this observation are discussed and a few suggestions are made as to the possible nature of the active site in this catalyst system. The material derived from the reduction of $VOPO_4 \cdot 2H_2O$ exhibited the highest catalyst activity by virtue of its optimised $(VO)_2P_2O_7$ morphology and high surface area. © 1996 Academic Press, Inc.

1. INTRODUCTION

Since the discovery that complex vanadium phosphorus oxides can be effective catalysts for the selective oxidation of *n*-butane to maleic anhydride (1), many articles concerning the performance of these catalysts have been published (2, 3). Several commercial methods have been devised to prepare the catalyst precursor compound $VOHPO_4 \cdot 0.5H_2O$, which is then subsequently transformed under reaction conditions to give the final "activated" catalyst. Initially, aqueous solvents were employed and HCl was used as the reducing agent to dissolve V_2O_5 (4). Subsequently, nonaqueous solvents were found to give improved catalysts and have now become the preferred media for the production of high activity catalysts. Examples of nonaqueous preparation routes include the use of isobutanol as the solvent and HCl as the reducing agent (5), or alternatively, the use of isobutanol as both solvent and reducing agent (6). More recently, a third class of preparative route involving the reduction of $VOPO_4 \cdot 2H_2O$, has been reported (7) which yields catalysts that are particularly effective for *n*-butane oxidation. Very recently, we published some results of a study in which we attempted to directly compare the performance and composition of vanadium phosphate catalysts produced by these three different preparation routes (8, 9). The work presented in this paper is an extension of our previous work, in which we compare the microstructure of the precursor phases and the activated catalysts prepared by these three routes. A number of other authors (10, 11) have also carried out limited microstructural comparisons of catalysts prepared by the more conventional aqueous and organic routes. Our more detailed observations in some instances confirm indirect deductions made by these previous authors, but in others they yield contradictory results. The underlying reasons for any disparities are discussed.

Activated vanadium phosphate catalysts are known to have a complicated microstructure often composed of a number of different crystalline phases. Amongst the phases which are possible (as identified by XRD) are

α_I-$VOPO_4$, α_{II}-$VOPO_4$, β-$VOPO_4$, γ-$VOPO_4$, δ-$VOPO_4$, $(VO)_2P_2O_7$ (vanadyl pyrophosphate), and $VO(PO_3)_2$.

Although the presence of these particular phases can be identified by techniques such as XRD and Raman spectroscopy (7, 12, 13), little is known about the morphology and distribution of these phases in the activated catalyst. Furthermore, trace amounts (i.e., <1%) of these phases which are below the detectability of the XRD or Raman spectroscopy techniques could easily be missed altogether. It is therefore surprising at first sight that this aspect of catalyst morphology has not previously been addressed using transmission electron microscopy. The underlying reason for this lies in the fact that most of these vanadium phosphate phases are prone to severe electron beam damage and will amorphise in a matter of a few seconds under normal imaging conditions. This renders the potentially

0021-9517/96 $18.00
Copyright © 1996 by Academic Press, Inc.
All rights of reproduction in any form reserved.

TABLE 1

Crystallographic and Morphological Data on Standard Phases

Compound	Crystal group[a]	Lattice parameters[a]/Å	Moisture sensitive[b]	Morphology[c,d]	Electron beam sensitivity[d]	Potential for HREM studies
$VOHPO_4 \cdot 1/2H_2O$ (hemihydrate)	Orthorhombic (Pmmn)	a = 7.416 b = 9.592 c = 5.689	No	Highly dependent on precise preparation route	High	Yes
α_I-$VOPO_4$	Tetragonal (P4/nmm)	a = 6.200 c = 4.110	Yes (45 min for hydration)	Platelets with (001) normal—Fig. 1a (TEM: featureless platelets)	High	Yes
α_{II}-$VOPO_4$	Tetragonal (Pnma)	a = 6.014 c = 4.434	Yes (10 h for hydration)	Platelets with (001) normal—Fig. 1b (TEM: platelets with distinctive surface texture)	High	Yes
β-$VOPO_4$	Orthorhombic (Pnma)	a = 7.770 b = 6.143 c = 6.965	No	Dense agglomerates of randomly oriented angular platelets—Fig. 1c	Low	Yes
γ-$VOPO_4$	Monoclinic (space-group unknown)	a = 9.64 b = 15.33 c = 16.62 $\beta = 95.04^\circ$	Yes (3 h for hydration)	Dense agglomerates of platelets showing "desert rose" type structure—Fig. 1d	Extreme	No
δ-$VOPO_4$	Orthorhombic (space-group unknown)	a = 6.260 b = 6.420 c = 9.090	Yes (3 h for hydration)	Random clusters of irregular platelets—Fig. 1e (TEM: platelets frequently exhibit parallel "slashes")	Extreme	No
$(VO)_2P_2O_7$ (pyrophosphate)	Orthorhombic ($Pca2_1$)	a = 7.725 b = 9.576 c = 16.576	No	Facetted needle-like crystals—Fig. 1f Basal (100) plane often exposed	Moderate	Yes

[a] Crystallographic data after Benabdelouahab [37] (Ph.D. thesis, I'ecole centrale de Lyon, 1994).
[b] Moisture sensitivity data after Benabdelouahab *et al*. [22] (*J. Catal.* **148**, 334 1994).
[c] Preparation routes described in Benabdelouahab *et al*. [21] (*J. Catal.* **134**, 151 1992).
[d] Microstructural data after Sajip [19] (M.Sc. thesis, University of Liverpool, 1994).

informative identification technique of microdiffraction to be impractical. In addition, distinguishing between the various $VOPO_4$ phases using microanalysis techniques such as energy dispersive X-ray analysis (EDX) or electron energy loss spectroscopy (EELS) is impossible because they have identical chemical compositions! Even distinguishing between $VOPO_4$, $(VO)_2P_2O_7$, and $VO(PO_3)_2$ by these microanalysis techniques is extremely difficult because of unfortunate peak overlaps in EELS and EDX spectra. The only compound which has previously undergone any significant TEM examination is the $(VO)_2P_2O_7$ phase (14–17) which is one of the more electron beam stable phases.

Recently, however, there has been a strong driving force to gain a detailed knowledge of the type and distribution of vanadium phosphate phases present in the activated catalyst because of the controversy which exists as to which phase or combination of phases are necessary for optimum catalytic behaviour. Some researchers favour a single compound $(VO)_2P_2O_7$ to be the sole active phase (18) and have indicated that the presence of other phases may be due to incomplete activation. However, a number of recent studies on vanadyl phosphate catalysts prepared in aqueous media have indicated that the additional presence of α_{II}-$VOPO_4$, γ-$VOPO_4$, and δ-$VOPO_4$ in the final catalyst is beneficial (12).

Recently we have shown by utilising low dose imaging techniques and an electronic recording system attached to our JEOL 2000EX HREM that we are able to distinguish between all these different phases in the transmission electron microscope (19, 20). Since we anticipated that the microstructure of "real activated" catalysts would be complicated to analyse we initially adopted a simpler approach whereby we used electron microscopy to characterise "pure standards" of all the aforementioned phases which had been previously prepared for a Raman spectroscopy characterisation study (21, 22). This has enabled us to compile a comprehensive "atlas" of standard phases. Each entry contains a selection of typical SEM, TEM, and HREM images of the pure standards, as well as any characteristic selected area diffraction patterns. Presented in Table 1 is a summary of relevant crystallographic data for each these phases, as well as some details of striking microstructural characteristics which can be used to identify the presence of a particular phase. As an illustration of the diversity of morphologies that the standard phases can adopt, we reproduce in Fig. 1, a representative SEM micrograph from each

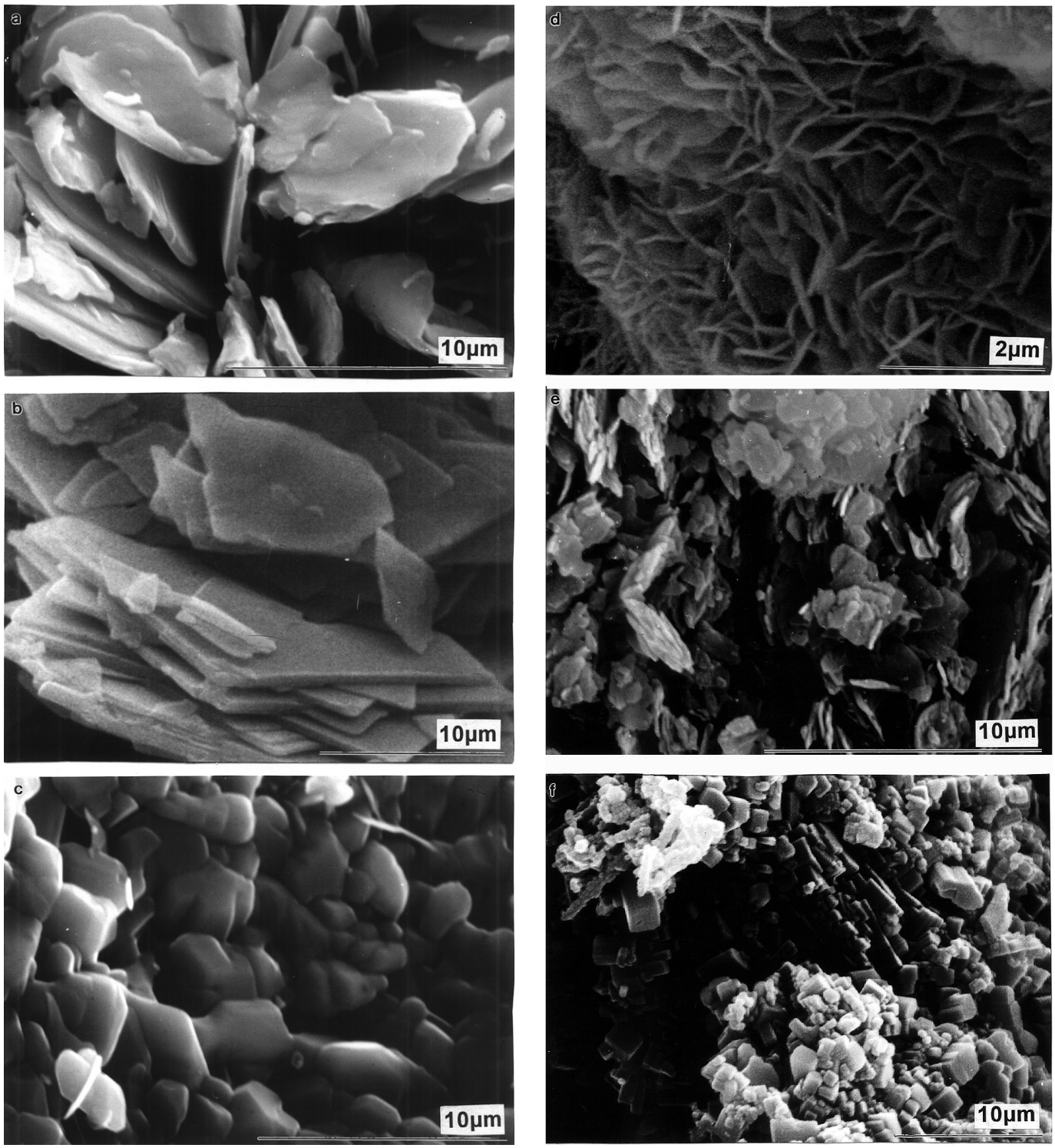

FIG. 1. Representative SEM micrographs from "standard" phases of (a) α_I-$VOPO_4$, (b) α_{II}-$VOPO_4$, (c) β-$VOPO_4$, (d) γ-$VOPO_4$, (e) δ-$VOPO_4$, and (f) $(VO)_2P_2O_7$.

of the standard phases. For instance, by studying this figure it is clear the α_I-$VOPO_4$ and α_{II}-$VOPO_4$ prefer platelike morphologies, whereas $(VO)_2P_2O_7$ appears to form more rectangular shaped crystallites.

The availability of such an atlas as a reference source has put us in the position, where for the first time, we can attempt to systematically analyse the microstructure of the more complex activated catalyst systems. In this article we present a detailed comparison of catalyst morphologies which develop from $VOHPO_4 \cdot 0.5H_2O$ precursors produced (i) in aqueous media, (ii) in nonaqueous media, and (iii) by the reduction of the $VOPO_4 \cdot 2H_2O$ dihydrate phase. Our observations are then discussed and correlated with the measured catalytic performances of the three activated catalysts. Finally a few suggestions are made as to the possible nature of the active site in this catalyst system.

2. EXPERIMENTAL

2.1. Catalyst Precursor Preparation and Catalyst Activation

Three distinct preparation routes, denoted VPA, VPO, and VPD, were considered in this study. Although these preparation procedures have previously been reported elsewhere (7, 8), brief details will be outlined here.

The *VPA precursor* was prepared in an "aqueous medium" by dissolving V_2O_5 (6.06 g) in aqueous HCl (35%, 79 ml) at reflux for 2 h. H_3PO_4 (8.91 g, 85%) was added and the solution refluxed for a further 2 h. The solution was subsequently evaporated to dryness and the resulting solid was refluxed in water (20 ml H_2O/g solid) for 1 h. It was then filtered hot, washed with warm water, and then dried in air (110°C, 16 h).

The *VPO precursor* was prepared in an "organic medium" by adding V_2O_5 (11.8 g) to isobutanol (250 ml). H_3PO_4 (16.49 g, 85%) was then introduced and the whole mixture was refluxed for 16 h. The light blue suspension was then separated from the organic solution by filtration and washed with isobutanol (200 ml) and ethanol (150 ml, 100%). The resulting solid was refluxed in water (9 ml/g solid), filtered hot, and dried in air (110°C, 16 h).

The *VPD precursor* was prepared via the dihydrate compound $VOPO_4 \cdot 2H_2O$. A mixture of V_2O_5 (11.8 g) and H_3PO_4 (115.5 g, 85%) were refluxed in water (24 ml/g solid) for 8 h. The resulting $VOPO_4 \cdot 2H_2O$ was recovered by filtration and washed with a little water. Some $VOPO_4 \cdot 2H_2O$ (4 g) was subsequently refluxed with isobutanol (80 ml) for 21 h, and the resulting solid was recovered by filtration and dried in air (110°C, 16 h).

The catalyst precursors were used in powder form and each was evaluated for the oxidation of *n*-butane in a standard laboratory microreactor. The precursors (1 g) were transformed *in situ* in the reactor to the final VPA, VPO, and VPD catalysts, respectively. Identical transformation conditions (385°C, 1000 h^{-1} GSHV, 1.5% butane in air, 75 h) were used for each. Their catalytic performances after activation were also compared. Reactor products were analysed using on-line chromatography. Carbon mass balances were typically 98–102% for all data cited.

2.2. Catalyst Characterisation

The precursor samples, as well as the catalysts after activation, were characterised using powder X-ray diffraction and scanning electron microscopy. In addition, the activated catalysts were subjected to detailed microstructural analysis using a combination of transmission electron microscopy and ^{31}P NMR spin echo mapping.

An Hitachi S-2460-N scanning electron microscope was employed to obtain topographical information from the specimens. Samples suitable for transmission electron microscopy analysis were prepared by dispersing the catalyst powder onto a lacey carbon film supported on a copper mesh grid. TEM observations were made in a JEOL 2000EX high resolution electron microscope operating at 200 kV. This instrument has been fitted with a low light level TV camera and frame-averaging system to allow us to use very low illumination conditions. This latter condition is essential for beam sensitive vanadium phosphate compounds. Images were recorded on S-VHS videotape, individual frames from which could be captured subsequently into a Macintosh Quadra computer for enhancement and detailed analysis.

The ^{31}P NMR measurements were performed on a BRUKER MSL 300 NMR spectrometer. The ^{31}P spin echo mapping method has been shown by Li *et al.* (23) and Sananes *et al.* (13) to be a very powerful technique for evaluating the relative proportions of V^{5+} and V^{4+} ions surrounding the P atoms in vanadium phosphate compounds. The ^{31}P NMR spin echo spectra were recorded under static conditions using a 90°x-t–180°y-t acquire sequence. The 90° pulse was 4.2 ms and t was 20 ms. For each sample the irradiation frequency was varied in increments of 100 kHz above and below the ^{31}P resonance of H_3PO_4. The number of spectra recorded was dictated by the frequency limits beyond which no spectral intensity was detectable. The ^{31}P NMR spin echo mapping information was then obtained by superposition of all the spectra.

3. RESULTS

3.1. Microstructural Characterisation of Catalyst Precursors

3.1.1. VPA Precursor

The BET surface area of the VPA precursor was 3 m^2g^{-1} and the SEM micrograph shown in Fig. 2(a) demonstrates that this material has a coarse platelike morphology. The platelets, which are typically 5 μm in diameter and less than

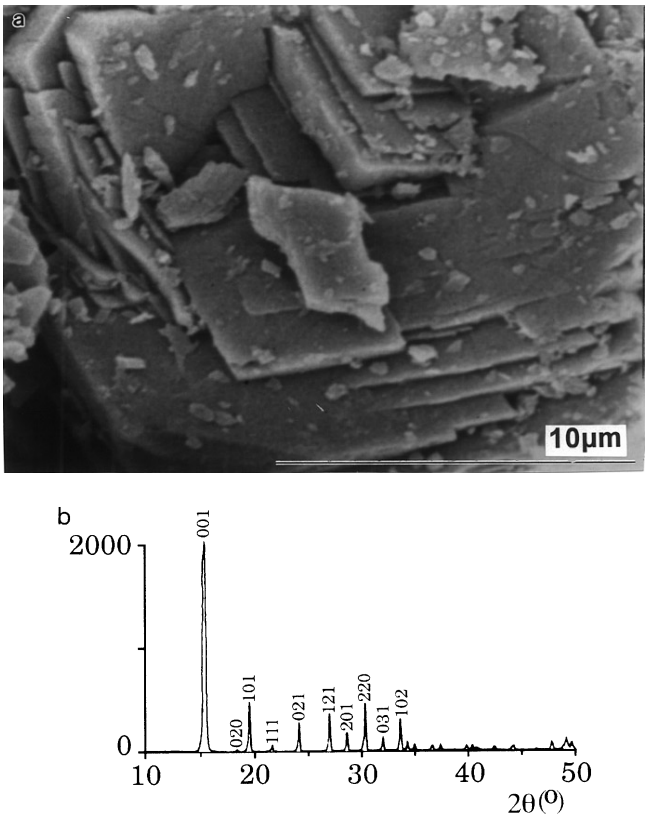

FIG. 2. (a) An SEM micrograph; (b) an XRD spectrum from VPA precursor material.

1 μm in thickness, are also seen to be decorated with more irregular shaped crystallites of sub-μm dimensions. The corresponding XRD spectrum from this sample is shown in Fig. 2(b) in which all the peaks can be indexed to the orthorhombic $VOHPO_4 \cdot 0.5H_2O$ (hemihydrate) structure. The 001 reflection shows an enhanced intensity which is consistent with the platelet normal being [001]. The propensity for the basal (001) plane of $VOHPO_4 \cdot 0.5H_2O$ to develop preferentially has been reported previously (15, 24).

3.1.2. VPO Precursor

The BET surface area of the VPO precursor was 11 m^2g^{-1} and the SEM micrograph presented in Fig. 3(a) shows that the material again has a platelike texture. The platelets are considerably smaller than those of the VPA precursor, with typical diameters of around 1 μm and thicknesses of less than 0.1 μm. It is also clear that the platelets have a light tendency to agglomerate to form structures resembling "flattened flowers" in which each "petal" corresponds to an individual platelet. Figure 3(b) shows the XRD spectrum from this sample in which all the reflections can be indexed to the $VOHPO_4 \cdot 0.5H_2O$ structure. The predominance of the (001) basal plane in the platelet structure again gives rise to an enhancement of the 001 peak intensity in the diffraction pattern.

3.1.3. VPD Precursor

The BET surface area of the VPD precursor was 32 m^2g^{-1} and the morphology of this material can be seen in the SEM micrograph in Fig. 4(a). The precursor is made up of platelets ($\sim$1 μm diameter and less that 0.1 μm in thickness) which are densely packed to form "rose-like" clusters. These characteristic agglomerates are roughly spherical in shape and have a diameter of about 2 μm. The XRD spectrum from the VPD precursor is shown in Fig. 4(b). Even though all the peaks in this spectrum can be assigned to the $VOHPO_4 \cdot 0.5H_2O$ structure, the relative peak intensities are very different from those shown in the corresponding spectra from the VPA and VPO precursors. In addition, the high level of background noise and the broad peak widths of the reflections in this spectrum suggest that the material is not fully crystalline and that a considerable degree of structural disorder is present.

3.2. Catalytic Performance Comparison

Table 2 summarizes the catalytic performance data on the VPA, VPO, and VPD materials after 75 h activation in a 1.5% *n*-butane/air mixture at 385°C. It is clear that the VPD material is considerably more catalytically active and selective to maleic anhydride as compared to the VPA and

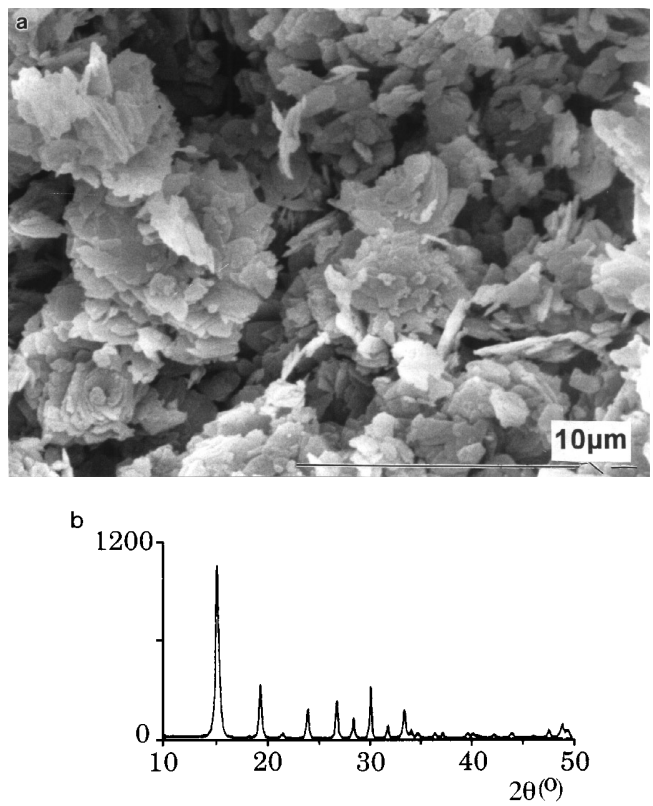

FIG. 3. (a) An SEM micrograph; (b) an XRD spectrum from VPO precursor material.

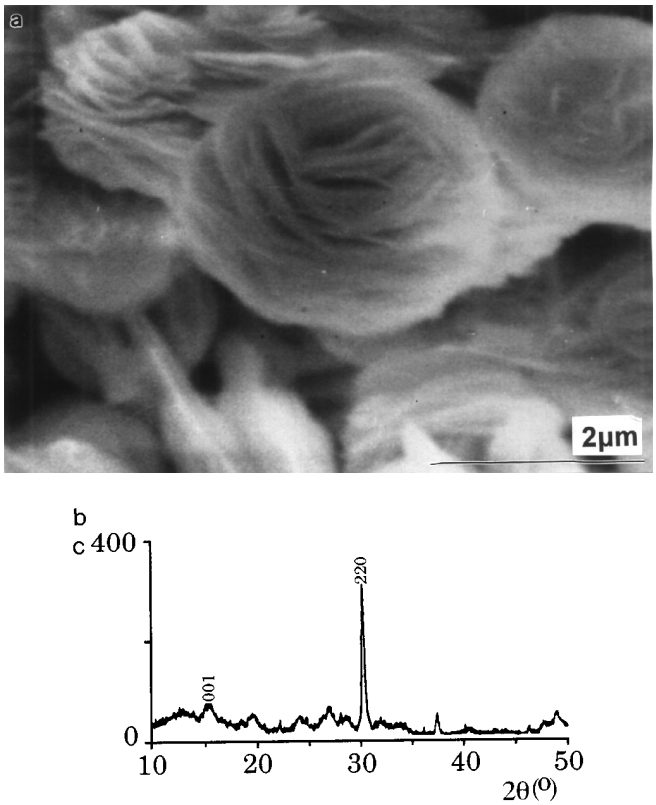

FIG. 4. (a) An SEM micrograph; (b) an XRD spectrum from VPD precursor material.

VPO catalysts. Since the three samples have virtually identical specific activities to maleic anhydride production, the enhanced catalytic performance of the VPD material can be ascribed to its high surface area (43 m^2g^{-1}) compared to the VPA and VPO catalysts (4 and 14 m^2g^{-1}, respectively). It is also noteworthy that the distribution of the catalytically active sites appears to be the same on the three catalysts (7).

3.3. Microstructural Characterisation of Final Catalysts

3.3.1. VPA Activated Catalyst

Figure 5(a) shows an SEM micrograph of the activated VPA catalyst. The large platelike crystals that comprised the precursor have clearly fractured on activation to give a mosaic of smaller crystallites (up to 1 μm in length) which have agglomerated to form larger particulates. XRD analysis of this material (Fig. 5(b)) showed it to contain a mixture of $VOPO_4$ phases. The strongest reflections present in this spectrum correspond to α_{II}-$VOPO_4$ and some weaker reflections characteristic of δ- and γ-$VOPO_4$ have also been indexed. No clear XRD evidence is present for the existence of the pyrophosphate phase, $(VO)_2P_2O_7$. The ^{31}P NMR spin echo mapping spectrum from the activated VPA catalyst is presented in Fig. 5(c). The strong signal at $\delta = 0$ ppm is indicative that the vast majority of the vanadium ions are in the 5^+ oxidation state, as found in $VOPO_4$. The much weaker signal at $\delta = 2600$ ppm suggests that some traces of $(VO)_2P_2O_7$ (i.e., V^{4+}) are also present.

TEM examination of the activated VPA catalyst revealed a complex microstructure. At least four distinct phases have been conclusively identified. The majority phase (constituting more than 80 vol% of the sample) consists of irregular shaped platelets which are usually about 1 μm in diameter (see Fig. 6(a)). Selected area diffraction patterns obtained normal to these platelets, as shown in Fig. 6(b), can be indexed to the [001] zone axis of α_{II}-$VOPO_4$. A second distinct morphology can be seen in Fig. 6(c), where characteristic arrays of parallel "splits" within the body of a platelet are observed. These particular platelets are much more beam sensitive than the α_{II}-$VOPO_4$ platelets and will amorphise in less than a second, even under low dose illumination conditions. These features are identical to those displayed by our standard sample of δ-$VOPO_4$ (19). The slashes are considered to be fissures occurring along specific crytallographic directions that have been generated when the precursor suddenly loses its water of hydration. The δ-$VOPO_4$ phase comprises about 10 vol% of the sample.

A third morphology which was found in the VPA specimens is shown in Fig. 6(d). This particular type of particle tended to show strong contrast because they were the least beam sensitive of all the phases present in this specimen, typically lasting about 10 s before complete amorphisation. They were usually elongated but fairly irregular in shape and ranged in size from 100 to 600 nm. A typical HREM image obtained from one of these particles

TABLE 2

Catalytic Performance Data

Catalyst	S_{BET}/m^2g^{-1} (Precursor)	S_{BET}/m^2g^{-1} (Activated Catalyst)	*n*-butane conversion/%	Product selectivity/%			Specific activity/ $\times 10^{-5}$ mol MA $m^{-2}h^{-1}$
				MA	CO	CO_2	
C1 (VPA)	3	4	11	51	41	7	1.24
C2 (VPO)	11	14	27	52	34	14	1.35
C3 (VPD)	32	43	62	64	21	14	1.19

Note. 75 h activation, 385°C, 1.5% *n*-butane/air, GSHV 1000 h^{-1}.

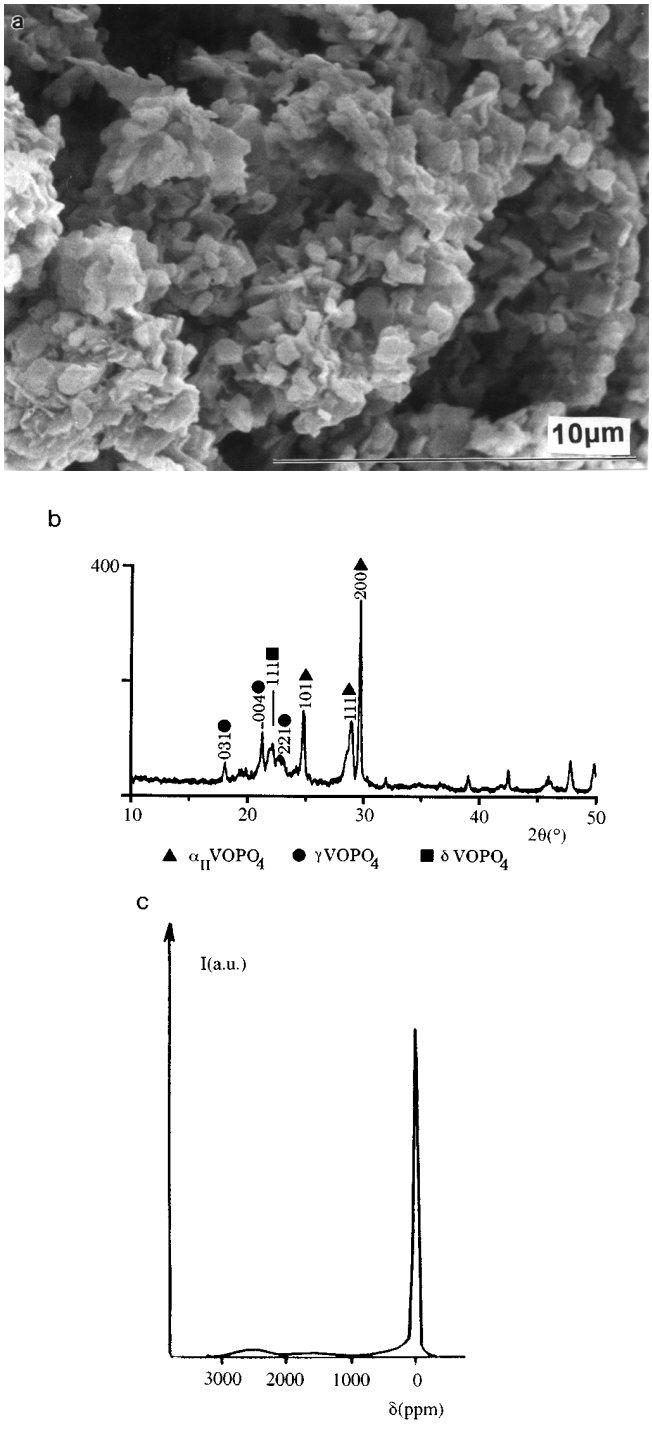

FIG. 5. (a) An SEM micrograph; (b) an XRD spectrum; (c) ^{31}P NMR spin echo mapping spectrum from the activated VPA catalyst.

is shown in Fig. 6(e). Analysis of these fringe spacings (0.39 and 0.42 nm) and intersection angles (90°) has allowed us to deduce that this corresponds to the [010] projection of $(VO)_2P_2O_7$ in which the $(\bar{2}00)$ and (004) lattice planes have been resolved. These crystalline $(VO)_2P_2O_7$ particles constitute less than 5% of the total sample volume.

A fourth much rarer morphology seen in the VPA catalyst is shown in Fig. 6(f), where a disordered grain is seen to exhibit elongated surface patches of a crystalline phase. Such elongated patches are also visible on a micrograph presented by Horowitz *et al* . (15), although the authors did not comment specifically on the existence or origin of these features. Similar particles to these were more commonly found in the VPD activated sample and are analysed in some detail in Section 3.3.3. It is sufficient at present to just state that these particles are thought to be the remnants of a hemihydrate particle which has only partially transformed to $(VO)_2P_2O_7$. A further point worthy of note, regarding the VPA sample, is that, even though our XRD data suggests the presence of γ-$VOPO_4$, we have not conclusively identified this phase in our TEM studies.

3.3.2. VPO Activated Catalyst

Figure 7(a) shows an SEM micrograph of the activated VPO catalyst. It still displays the "flattened-rose" type morphology that was exhibited by its corresponding precursor material, suggesting that a topotactic transformation may have occurred. The XRD spectrum obtained from this sample (shown in Fig. 7(b)) suggests that it is poorly crystallized, since no characteristic peaks can be easily indexed. This surprising deduction is consistent with previous laser raman spectroscopy studies (9) of this material. The ^{31}P NMR spin echo mapping spectrum of the activated VPO catalyst (Fig. 7(c)) shows a strong signal at $\delta = 0$ ppm (corresponding to $VOPO_4$ phases). It also exhibits a weak peak at 2600 ppm and a broad signal between 400 and 3000 ppm which has been interpreted as being characteristic of crystalline and disorganised $(VO)_2P_2O_7$, respectively.

A typical TEM micrograph obtained from the activated VPO catalyst is shown in Fig. 8(a). Three distinct structures are clearly discernable. The large plate-like grains, which are 1–2 μm in diameter, are amorphous in nature and are believed to correspond to the disorganised $(VO)_2P_2O_7$ phase. The surfaces of these platelets are decorated with rectangular (and sometimes square) crystallites showing strong diffraction contrast. These range from 50 to 200 nm in length and are stable enough to give good HREM images. Two characteristic lattice fringe patterns are commonly observed from the oblong particles. The first, shown in Fig. 8(b), exhibits 0.38 nm and 0.32 nm fringes that intersect each other at 90°. These correspond to the (200) and $(02\bar{4})$ lattice plane spacings of $(VO)_2P_2O_7$ when viewed along the [021] projection. The second characteristic lattice fringe pattern is shown in Fig. 8(c), where perpendicular sets of fringes with 1.66 and 0.96 nm periodicities are apparent. This corresponds to the [100] projection of $(VO)_2P_2O_7$, where the (001) and (010) lattice planes are resolved. Hence, this has allowed us to deduce that the oblong $(VO)_2P_2O_7$ crystallites are preferentially exposing

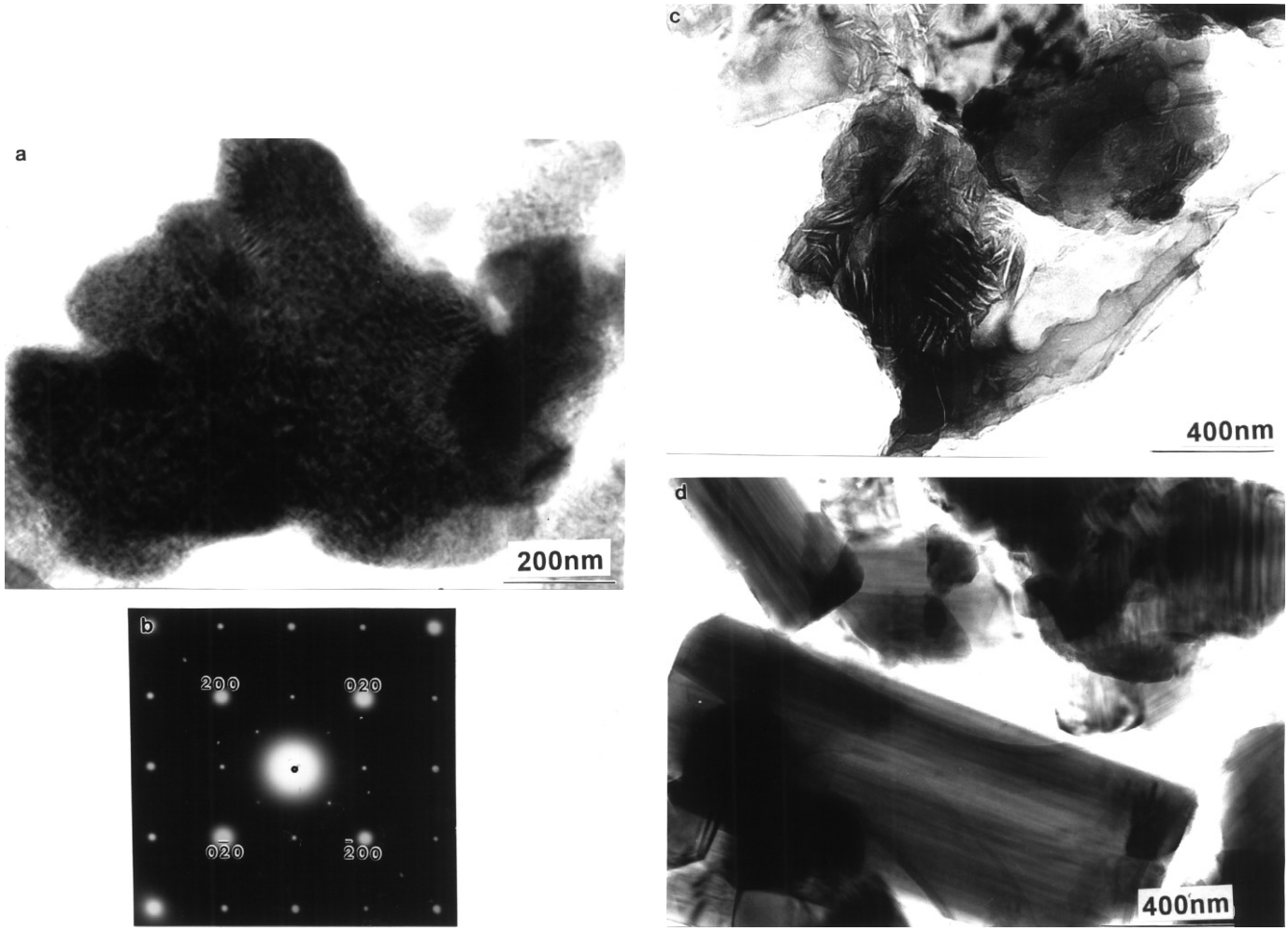

FIG. 6. Transmission electron micrographs from the VPA activated catalyst: (a) bright field micrograph of α_{II}-$VOPO_4$; (b) [001] selected area diffraction pattern from an α_{II}-$VOPO_4$ platelet; (c) bright field micrograph of a δ-$VOPO_4$ platelet; (d) bright field micrograph of a $(VO)_2P_2O_7$ crystallite; (e) an axial [010] HREM image from $(VO)_2P_2O_7$; (f) bright field micrograph of disordered $(VO)_2P_2O_7$ grain showing crystalline surface patches.

(100), (021), and $(0\bar{1}2)$ faces as shown in the schematic diagram in Fig. 8(d).

Characteristic "split" μm-size platelets are also commonly found in the activated VPO catalysts as indicated in Fig. 8(a). These very beam sensitive crystallites, which are similar to those observed in the VPA sample, constitute about 20 vol% of the sample and are typical of δ-$VOPO_4$.

3.3.3. VPD Activated Catalyst

Figure 9(a) shows an SEM micrograph of the VPD activated catalyst. A topotactic transformation has obviously occurred, since the activated material has retained the characteristic rosette-like structure of the precursor material. The activated catalyst does, however, also show occasional isolated platelets with 1 μm dimensions (as indicated in Fig. 9(a)). The XRD spectrum from this material is shown in Fig. 9(b), in which all the reflections can be indexed to the $(VO)_2P_2O_7$ structure. A broadening of the 200 reflection is characteristic of this catalyst. This is a consequence of (i) the overlap of the 200 with the 102 and 040 reflections and (ii) the development of a platelike morphology with a [100] platelet normal. Any $VOPO_4$ phases, if present, are below the detectability limit of the XRD technique. The complimentary ^{31}P NMR spin echo mapping data from this material is shown in Fig. 9(c). The spectrum is characteristic of crystallized $(VO)_2P_2O_7$ (signal at $\delta = 2600$ ppm) with a small amount of $VOPO_4$ (as deduced from the small signal at $\delta = 0$). The shoulder at 200–1800 ppm is thought to be indicative of the presence of a disorganised V^{4+} structure.

TEM examination of the final catalyst showed a combination of large isolated platelets and rosette shaped clusters as shown in Fig. 10(a). Selected area diffraction patterns obtained at normal incidence to the isolated platelets always gave a characteristic square geometry pattern which could

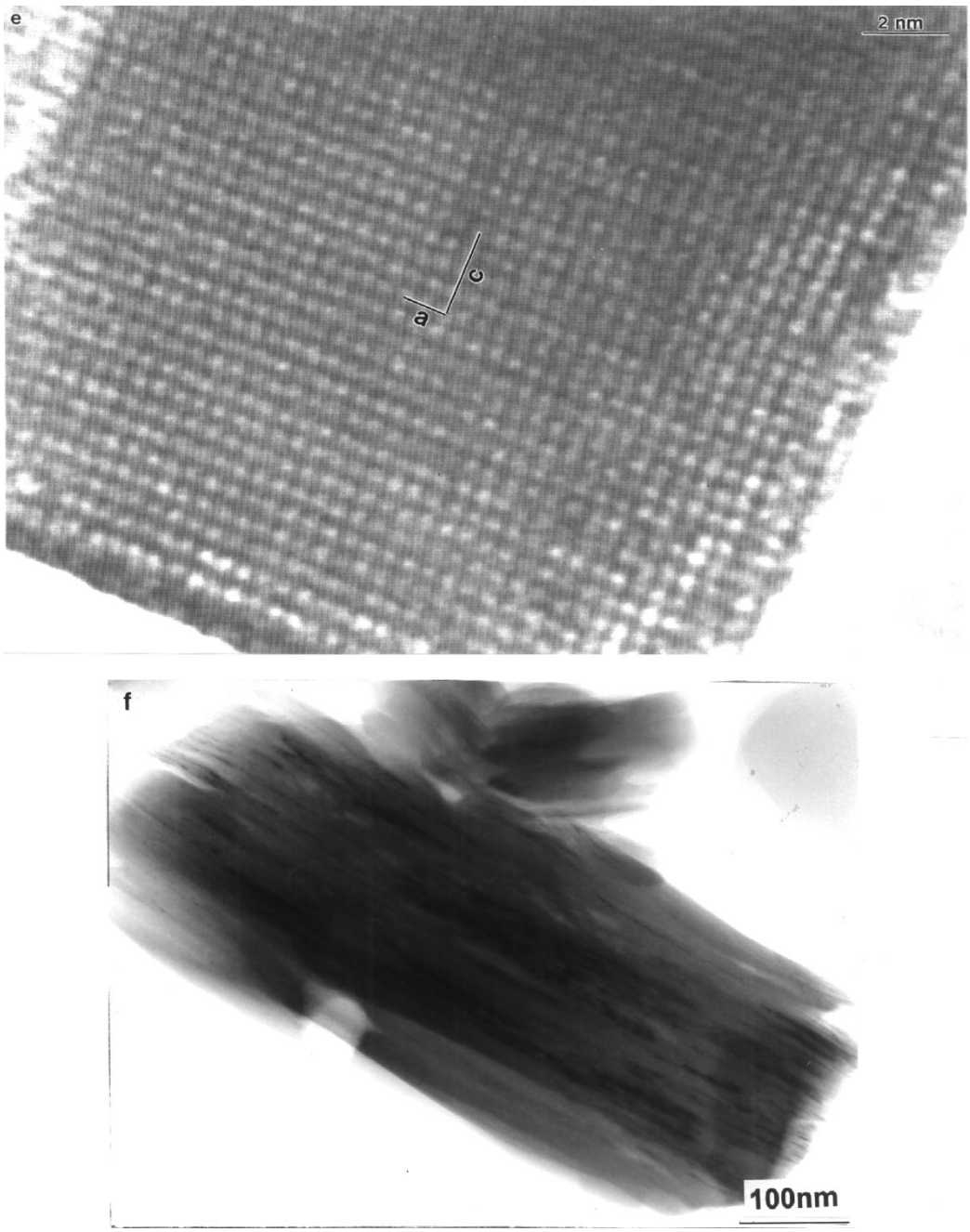

FIG. 6—*Continued*

be indexed to the [001] zone axis of α_{II}-$VOPO_4$. The corresponding HREM micrograph shown in Fig. 10(b) shows an [001] image in which the 200 and 020 lattice spacings (both 0.3 nm) of α_{II}-$VOPO_4$ are resolved. These α_{II}-$VOPO_4$ platelets accounted for about 3–4 vol% of the sample.

The rosette-type agglomerates, which at ~95 vol% constitute the majority phase, have been studied by HREM. Lattice images, such as that shown in Fig. 10(c), were obtained from the tips of individual "edge-on" crystallites. Analysis of fringe spacings (0.386 nm ($d_{\bar{2}00}$) and 0.414 nm (d_{004})) and intersection angles (90°) has allowed us to identify the image as the [010] projection of $(VO)_2P_2O_7$. In addition, an HREM image of one of these crystallites, obtained in a direction normal to the platelet, is presented in Fig. 10(d). The fringe structure (crossed 1.66 and 0.96 nm fringes with a 90° intersection angle) is consistent with that expected from the [100] projection of $(VO)_2P_2O_7$. Hence, the rosette-type structures are made up from agglomerates of $(VO)_2P_2O_7$ platelets that are preferentially exposing (100) crystal planes. It is interesting to note that small

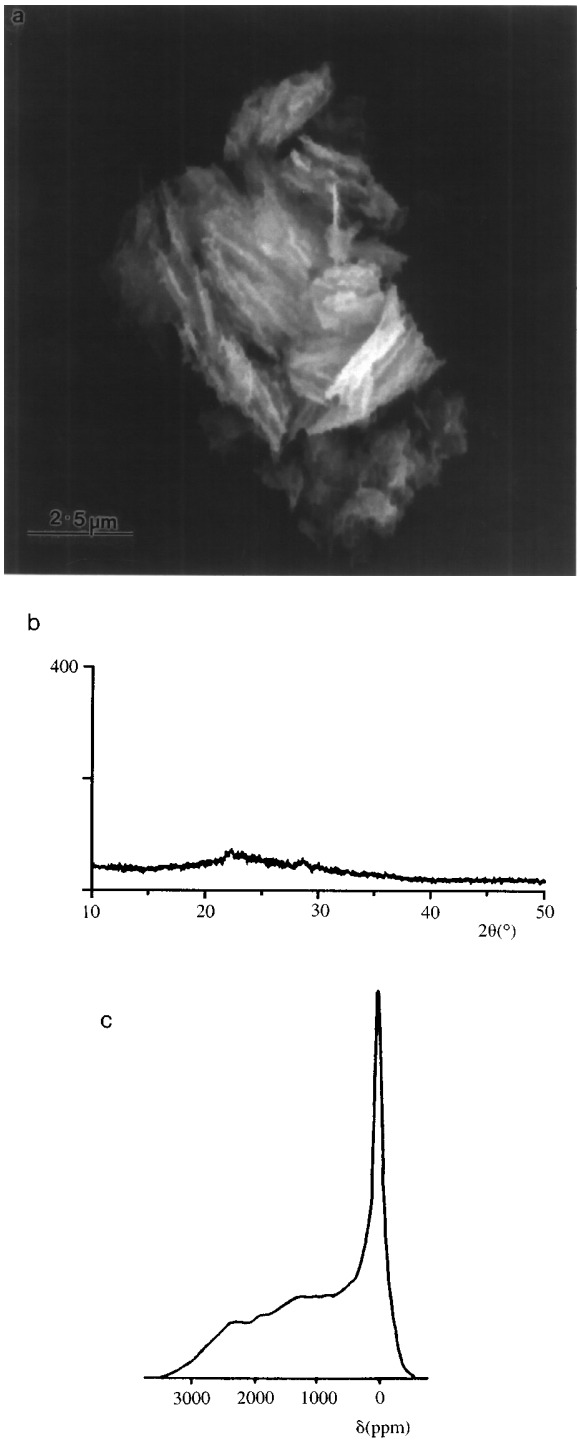

FIG. 7. (a) An SEM micrograph; (b) an XRD spectrum; and (c) ^{31}P NMR spin echo mapping spectrum from the activated VPO catalyst.

fragments of $(VO)_2P_2O_7$ (typically less than 400 nm in size) are sometimes seen to be supported in random orientations on the α_{II}-$VOPO_4$ platelets. These fragments have presumably spalled-off from the rosette clusters during catalyst activation. In fact, there is supporting evidence for spalling in Fig. 10(c), where the edge-on $(VO)_2P_2O_7$ platelet appears to be "cleaving" between two adjacent (100) planes.

A third morphology (see Fig. 11(a)) has also been observed in the activated VPD sample. These platelets, which are typically about 0.1–0.2 μm in size, are more beam sensitive and structurally disordered than either of the previously described $(VO)_2P_2O_7$ or α_{II}-$VOPO_4$ phases. Elongated raft-like patches of a second phase were always seen on the surface of these platelets. The typical dimensions of these patches were about 15×5 nm. In addition, on any platelet, the long dimensions of the patches were aligned suggesting that an orientation relationship exists between the support and the second phase. When observed by HREM, the surface patches were always found to be much more stable (i.e., a 5–10 s lifetime) under the electron beam than the underlying platelet. A typical HREM image of a surface patch is shown in Fig. 11(b) in which a 0.38 nm ($d_{\bar{2}00}$) set of fringes runs parallel to the long axis and a 0.32 nm ($d_{02\bar{4}}$) set of fringes runs in the perpendicular direction. These fringe separations and intersection angles correspond reasonably well with those expected from the [021] projection of $(VO)_2P_2O_7$. Hence, we suspect that the third morphology may correspond to the remnants of a hemihydrate particle which has only partially transformed to $(VO)_2P_2O_7$.

4. DISCUSSION

In this work we have applied XRD, ^{31}P NMR spin echo mapping and electron microscopical methods to study a series of activated vanadium phosphate catalysts. The use of any one of these techniques in isolation gives useful structural information on the catalyst. However, we have demonstrated that a combination of all three is necessary to gain a more complete picture of the overall microstructure. Furthermore, detailed structural assessments of these vanadium phosphate materials when correlated with catalytic performance measurements may eventually allow us to elucidate the precise roles of the $(VO)_2P_2O_7$ and various $VOPO_4$ phases in the catalytic process.

Some researchers favour a single compound, $(VO)_2P_2O_7$, to be the active phase (18) and have indicated that the presence of other phases may be due to incomplete activation. On the other hand, some studies indicate that a combination of phases is beneficial. For example, an early patent disclosure reported that catalysts containing α_{II}-$VOPO_4$ in addition to $(VO)_2P_2O_7$ were more active and the increase in activity was related to the amount of α_{II}-$VOPO_4$ phase present (25). Further evidence to confirm that the combination of $(VO)_2P_2O_7$ and α_{II}-$VOPO_4$ is beneficial is provided by the observation that pure α_{II}-$VOPO_4$ is not very selective for maleic anhydride formation (26, 27) (although it is active for butane oxidation) and that pure $(VO)_2P_2O_7$ is not very active (28).

FIG. 8. Transmission electron micrographs from the VPO activated catalyst: (a) bright field micrograph showing disordered $(VO)_2P_2O_7$ (x), δ-$VOPO_4$ (y) platelets and rectangular crystallites of $(VO)_2P_2O_7$ (z); (b) an axial HREM image from the [021] projection of $(VO)_2P_2O_7$; (c) an axial HREM image from the [100] projection of $(VO)_2P_2O_7$; (d) schematic diagram showing the morphology of the rectangular $(VO)_2P_2O_7$ crystallites.

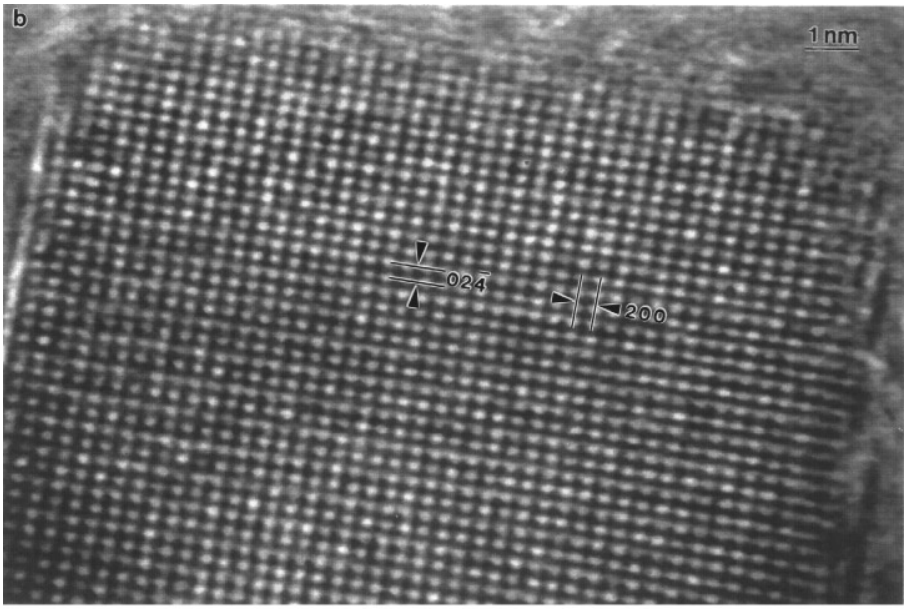

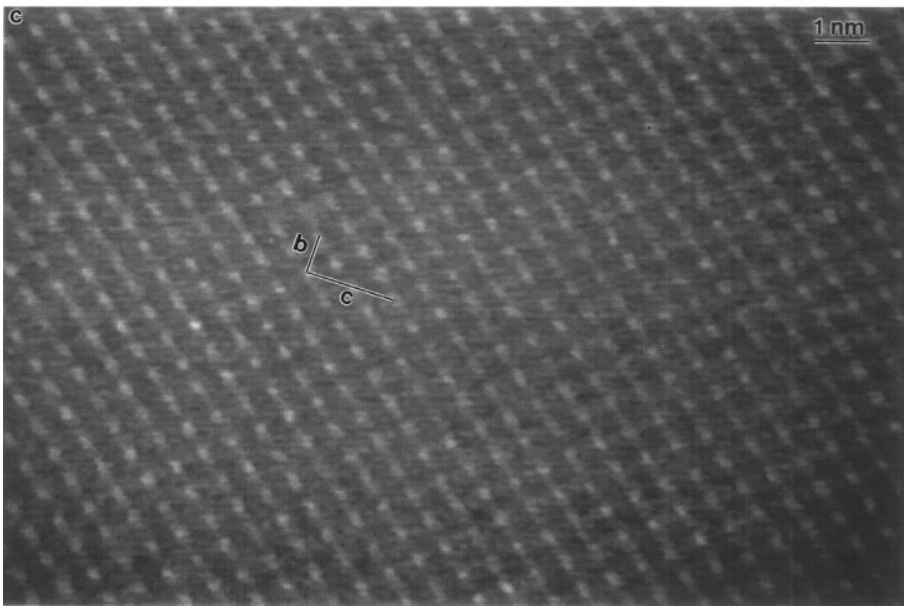

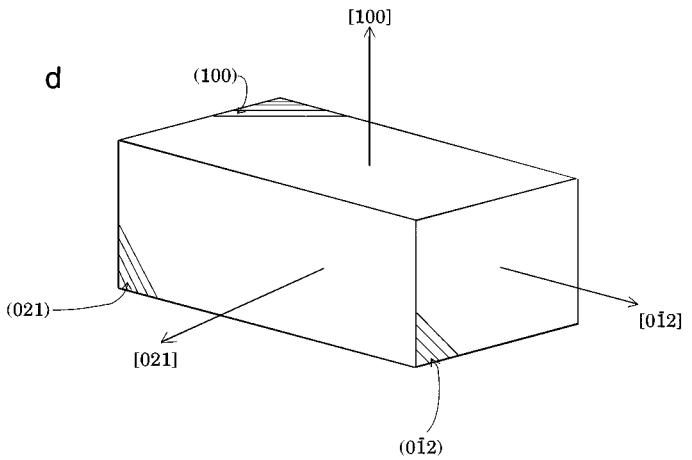

FIG. 8—*Continued*

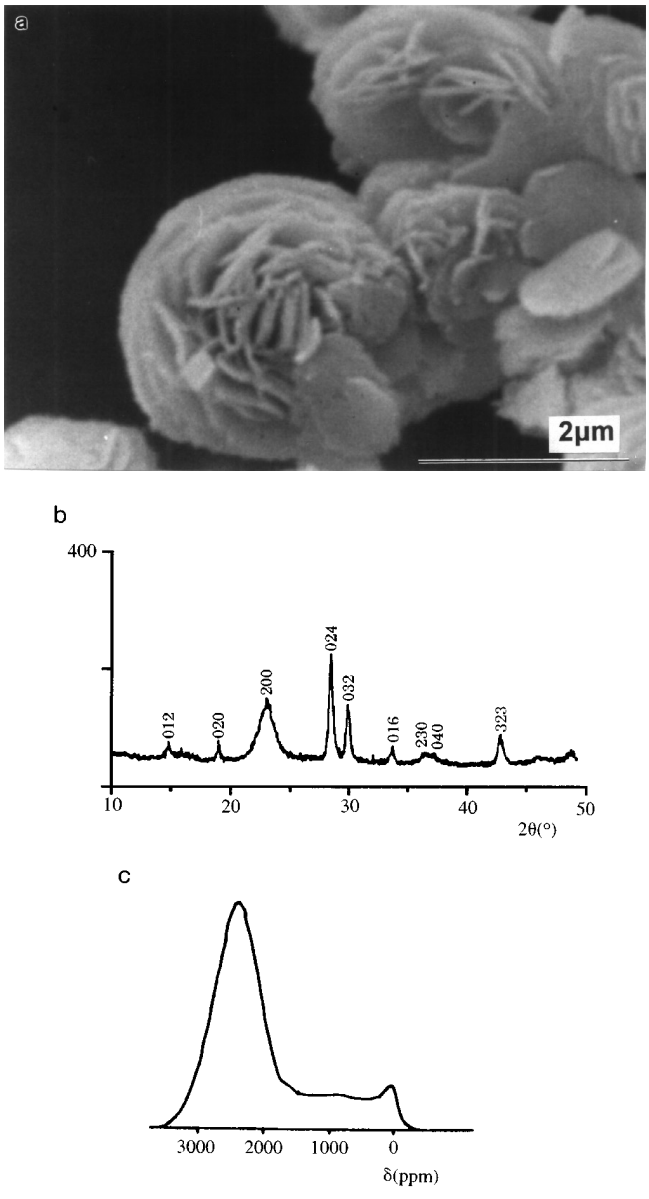

FIG. 9. (a) An SEM micrograph; (b) an XRD spectrum; and (c) ^{31}P NMR spin echo mapping spectrum from the activated VPD catalyst.

In-situ Raman spectroscopy studies (12) have recently demonstrated that during the course of the activation of the hemihydrate precursor, α_{II}-$VOPO_4$, δ-$VOPO_4$, and $(VO)_2P_2O_7$ appear simultaneously and this event coincides with the initial formation of maleic anhydride. Systematic studies on the pure $VOPO_4$ phase have demonstrated that δ-$VOPO_4$ is both active and selective for maleic anhydride formation (29). The overall situation is further complicated by the fact that many recent publications on this topic refer to the presence of a disordered $(VO)_2P_2O_7$ phase (9) whose role in the catalytic process is even more uncertain.

In this work we have clearly demonstrated that variations in the preparation procedure of the precursor phase, $VOHPO_4 \cdot 0.5H_2O$, can lead to activated catalysts with very different microstructures:

The *VPA material*, derived from a precursor prepared in an aqueous medium, predominantly yields platelets of α_{II}-$VOPO_4$ along with smaller amounts of δ-$VOPO_4$ and $(VO)_2P_2O_7$. This is contrary to the observations of Busca *et al*. (10) and Cornaglia *et al*. (11) who only observed characteristic $(VO)_2P_2O_7$ diffraction peaks in XRD patterns obtained from their VPA material. This anomaly may be a consequence of the fact that the latter catalysts were subjected to longer activation times, higher activation temperatures, and higher butane/air GSHV values, as well as additional pretreatment steps prior to activation. It is worth noting, however, that these authors did deduce the presence of trace amounts of unidentified $VOPO_4$ phases from techniques such as ^{31}P NMR spin echo mapping and FTIR.

The *VPO material*, derived from a precursor prepared in an organic medium, predominantly yields disordered $(VO)_2P_2O_7$ platelets, along with some δ-$VOPO_4$ and regular shaped crystallites of $(VO)_2P_2O_7$. The observation of significant structural disorder in VPO catalysts is largely consistent with previous studies (10, 11, 29) and is thought to be related to the retention of alcohol between (200) planes in the pyrophosphate structure. Trace amounts of an unidentified $VOPO_4$ phase were also detected by FTIR in the previous studies, which we have shown to be δ-$VOPO_4$.

The *VPD material*, derived by the reduction of $VOPO_4 \cdot 2H_2O$, gives rise to characteristic rosette-type agglomerates of $(VO)_2P_2O_7$, along with a minor amount of α_{II}-$VOPO_4$.

There is also clear evidence that all three of these catalysts showed that presence of "partially transformed" $(VO)_2P_2O_7$. This may be a consequence of the activation time being 75 h, rather than the full 1000 h, often quoted as being necessary for full equilibration (30). It should be stressed that after 75 h of activation our catalysts were found to have a stable catalytic performance with the activity and selectivity expected for a nonpromoted catalyst derived from $VOHPO_4 \cdot 0.5H_2O$.

A very curious point which emerges from our investigation is that, although the VPA, VPO, and VPD catalysts all contain very different volume fractions of the various phases, their specific activities are virtually identical. This seems to suggest that the distribution of catalytically active sites is the same for all the materials. From our observations one could postulate that the surfaces of *all* these phases may be active. Furthermore, the relationship between morphology and activity could be so complex that the resulting similarity in specific activities that we have measured may just be a coincidence!

It may also be important to recognise that the only phase present in all the materials, albeit with widely differing volume fraction, is $(VO)_2P_2O_7$. In the VPO material the crystalline $(VO)_2P_2O_7$ adopts a regular oblong morpho-

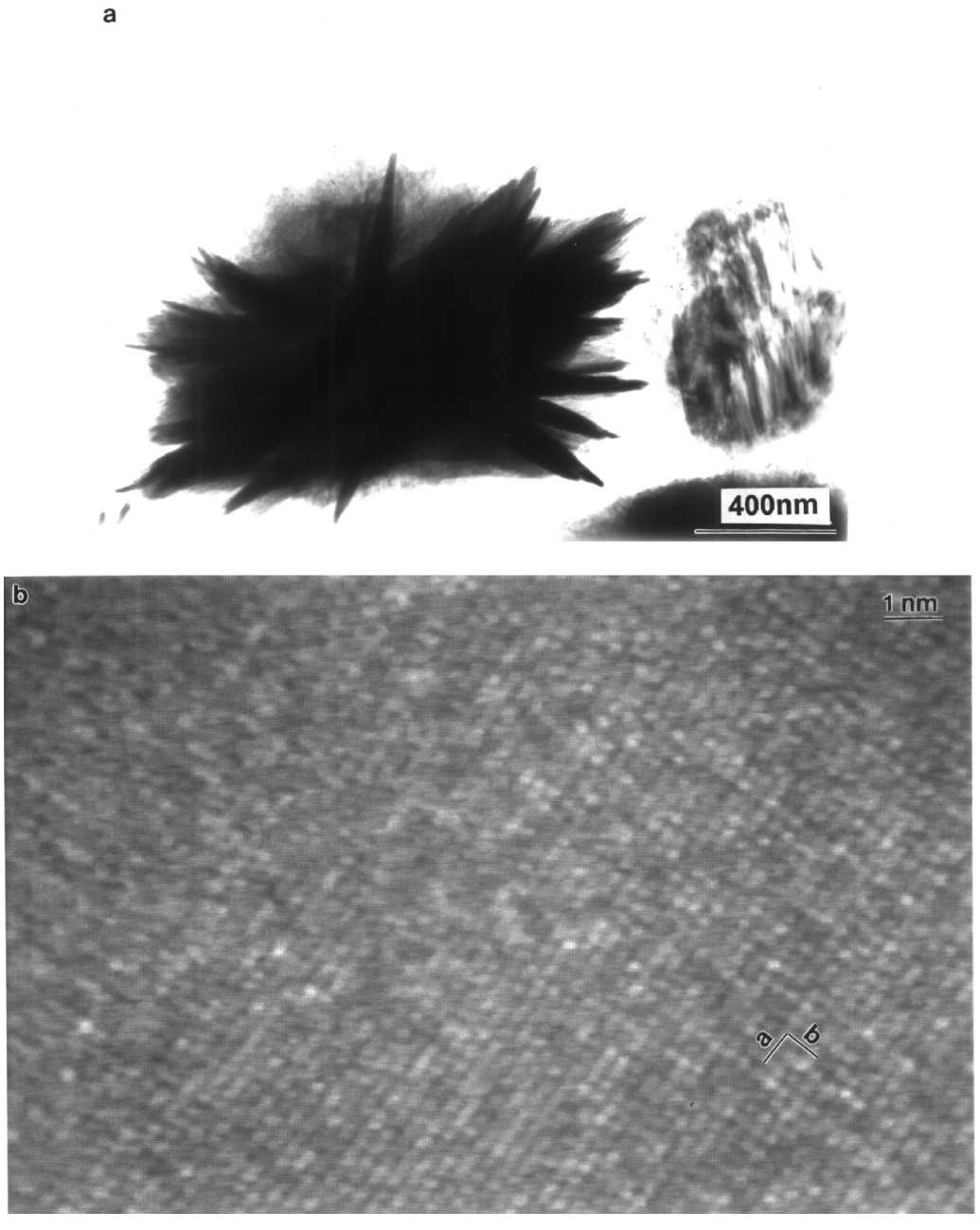

FIG. 10. Transmission electron micrographs from the VPD activated catalyst: (a) bright field micrograph showing rosette-type structures of $(VO)_2P_2O_7$ and isolated platelets of α_{II}-$VOPO_4$; (b) an axial HREM image from the [001] α_{II}-$VOPO_4$; (c) an [010] $(VO)_2P_2O_7$ lattice image obtained edge-on from a rosette platelet; (d) an [100] $(VO)_2P_2O_7$ lattice image obtained perpendicular to a rosette platelet.

logy exposing (100), (021), and $(01\bar{2})$ crystal faces. In the VPA material, the $(VO)_2P_2O_7$ exists with a much more irregular morphology. In the VPD material, the majority $(VO)_2P_2O_7$ phase shows a very high surface area platelet morphology preferentially exposing (100) surfaces. Since the (100) plane of $(VO)_2P_2O_7$ has been previously shown to have the best catalytic properties for maleic anhydride formation (31), the morphology displayed by the VPD material is approaching optimal as far as the $(VO)_2P_2O_7$ phase is concerned.

The precise nature of the active site in vanadium phosphorus oxide catalysts is still a matter of much controversy. It is now generally accepted that the active catalyst requires the presence of both V^{4+} and V^{5+} cations in close proximity. Electron microscopy studies may indeed allow us to make some progress in identifying the true nature of

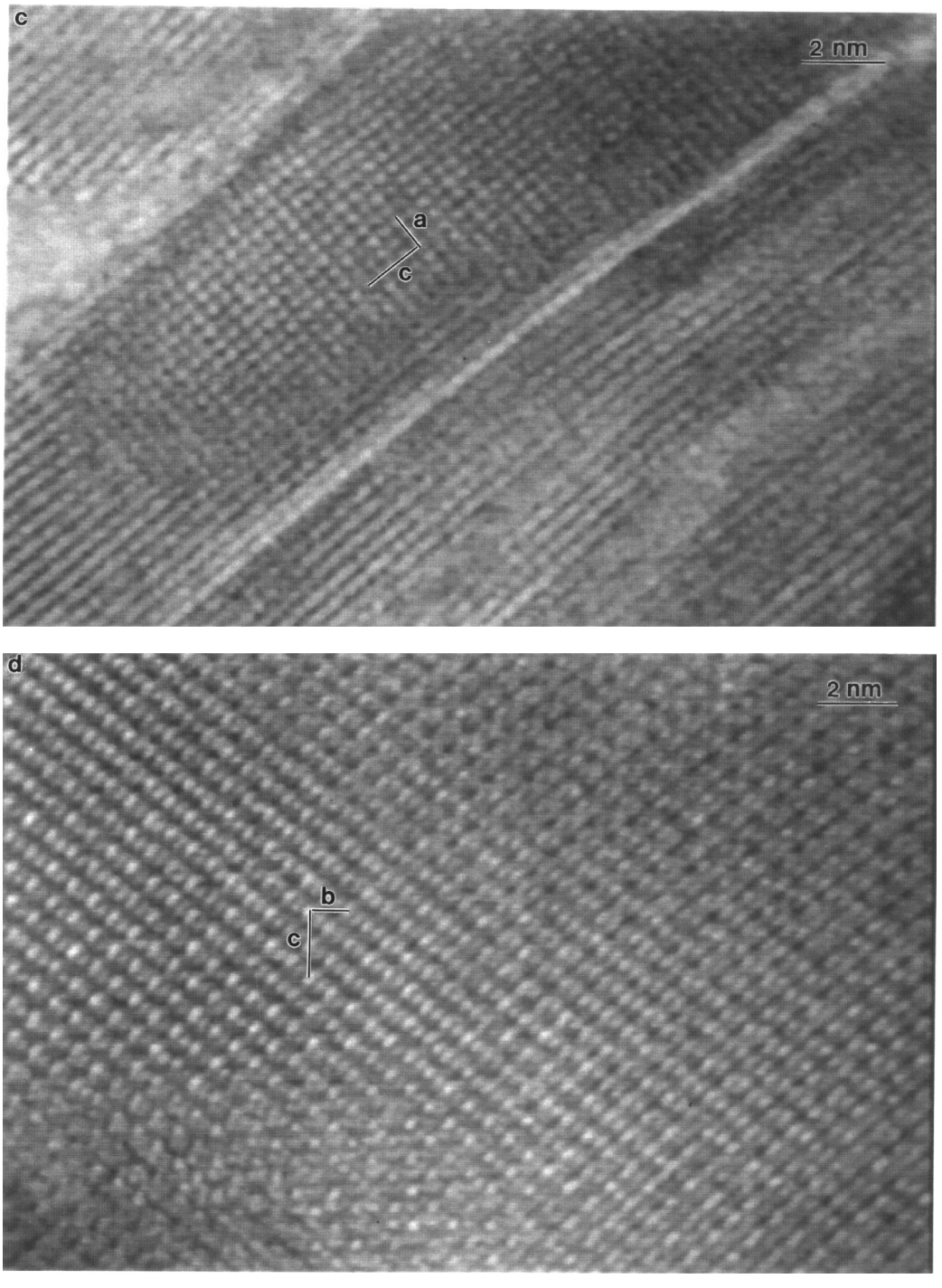

FIG. 10—*Continued*

the active site. Several authors (32–35) have suggested that the activated $(VO)_2P_2O_7$ phase exhibits some "domains" of $VOPO_4$-type phases on its surface and that the V^{5+}/V^{4+} couple exists at the periphery of these islands. Gai and Kourtakis (36) have very recently performed some severe reductions of the $(VO)_2P_2O_7$ phase *in situ* in the electron microscope and observed surface modification accompanied by the formation of extended shear defects. These latter defects, if present under normal reaction conditions, could also be sites where V^{5+} and V^{4+} ions co-exist. We are currently attempting similar *ex-situ* environmental cell experiments on our VPA, VPO, and VPD materials in which we are employing reaction conditions much closer to those encountered under catalyst activation situations.

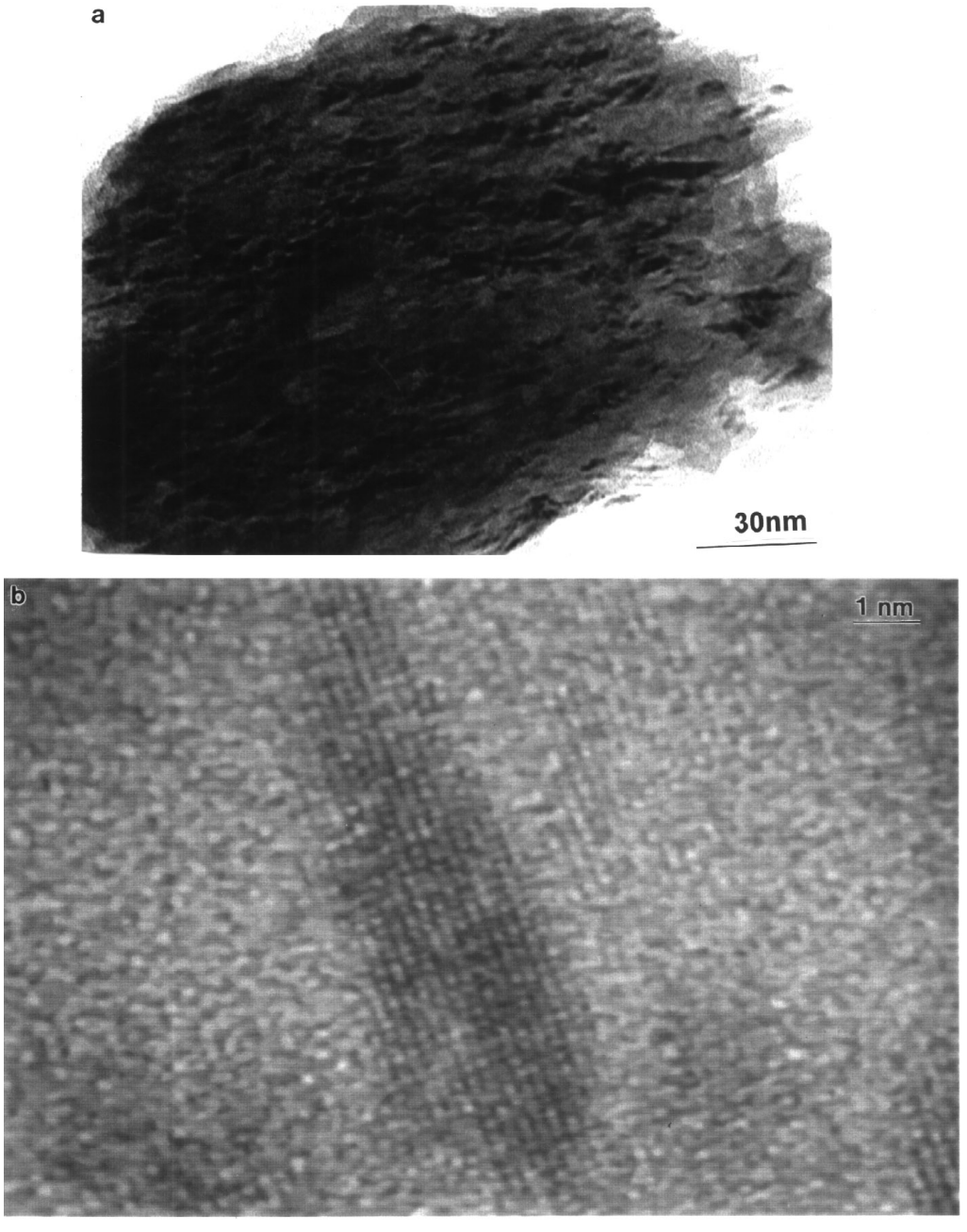

FIG. 11. A disordered $(VO)_2P_2O_7$ grain showing crystalline surface patches. The lattice image from a crystalline patch in (b) corresponds to the [021] projection of $(VO)_2P_2O_7$.

ACKNOWLEDGMENTS

We thank the European Human Capital Mobility Programme (Contract CHRX-CT92-0065) and the EPSRC for financial support.

REFERENCES

1. Bergman, R. L., and Frisch, N. W., U.S. Patent, 3,293,268 (1968), assigned to Princeton Chemical Research.
2. Centi, G., *Catal. Today* **18**, 1 (1994).
3. Hutchings, G. J., *Appl. Catal.* **72**, 1 (1991).
4. Harrison, J. P., U.S. Patent No. 3,985,775 (1976).
5. Sneider, R. A., U.S. Patent No. 3,864,280; U.S. Patent No. 4,043,943 (1977).
6. Johnson, J. W., Johnston, D. C., Jacobsen, A. J., and Brady, J. F., *J. Am. Chem. Soc.* **106**, 8123 (1984).
7. Hutchings, G. J., Olier, R., Sananes, M. T., and Volta, J.-C., *in* "Proceedings, Second World Congress, Fourth European Workshop Meeting, New Developments in Selective Oxidation, Bunalmadena, Spain, September 20–24, 1993."
8. Hutchings, G. J., Olier, R., Sananes, M. T., and Volta, J.-C., *Stud. Surf. Sci. Catal.* **82**, 213 (1994).

9. Sananes, M. T., Tuel, A., Hutchings, G. J., and Volta, J.-C., *J. Catal.* **148**, 395 (1994).
10. Busca, G., Cavani, F., Centi, G., and Trifiro, F., *J. Catal.* **99**, 400 (1986).
11. Cornaglia, L. M., Caspani, C., and Lombardi, E. A., *Appl. Catal.* **74**, 15 (1991).
12. Hutchings, G. J., Desmartin-Chomel, A., Olier, R., and Volta, J.-C., *Nature* **368**, 41 (1994).
13. Sananes, M. T., Tuel, A., and Volta, J.-C., *J. Catal.* **145**, 251 (1994).
14. Bordes, E., and Courtine, P., *J. Catal.* **57**, 236 (1979).
15. Horowitz, H. S., Blackstone, C. M., Sleight, A. W., and Teufer, G., *Appl. Catal.* **38**, 211 (1988).
16. Ruiz, P., Bastians, Ph., Cassin, L., Reuse, R., Daza, L., Acosta, D., and Delmon, B., *Catal. Today* **16**, 39 (1993).
17. Guliants, V. V., Benzinger, J. B., Sunderasan, S., Yao, N., and Wachs, I. E., *Catal. Lett.* **32**, 379 (1995).
18. Ebner, J. R., and Thompson, M. R., *Catal. Today* **18**, 51 (1994).
19. Sajip, S., MSc(Eng) thesis, University of Liverpool, 1994.
20. Kiely, C. J., Sajip, S., Ellison, I. J., Sananes, M. T., Hutching, G. J., and Volta, J-C., *Catal. Lett.* **33**, 357 (1995).
21. Benabdelouahab, F., Olier, R., Guilhaume, N., Lefebvre, F., and Volta, J-C., *J. Catal.* **134**, 151 (1992).
22. Benabdelouahab, F., Volta, J.-C., and Olier, R., *J. Catal.* **148**, 334 (1994).
23. Li, J., Lashier, M. E., Schrader, G. L., and Gerstein, B. C., *Appl. Catal.* **73**, 83 (1991).
24. Centi, G., (Ed.), "Forum on Vanadyl Pyrophoshate Catalysts," *Catalysis Today* Vol. **16**, Elsevier, Amsterdam, 1993.
25. Hutchings, G. J., and Higgins, R., U. K. Patent 1,601,121 (1981) assigned to Imperial Chemical Industries.
26. Morselli, L., Trifero, F., and Urban, L., *J. Catal.* **75**, 112 (1982).
27. Zhang-Lin, Y., Forissier, M., Sneedon, R. P., Vedrine, J. C., and Volta, J.-C., *J. Catal.* **145**, 256 (1994).
28. Moser, T. P., and Scrader, G. L., *J. Catal.* **92**, 216 (1985).
29. Zhang-Lin, Y., Forissier, M., Vedrine, J. C., and Volta, J.-C., *J. Catal.* **145**, 267 (1994).
30. Lombardo, E. A., Sanchez, C. A., and Cornaglia, L. M., *Catal. Today* **15**, 407 (1992).
31. Bordes, E., *Catal. Today* **1**, 499 (1987).
32. Centi, G., *Catal. Today* **16**, 5 (1993).
33. Hodnett, B. K., *Catal. Today* **1**, 447 (1987).
34. Centi, G., Trifero, F., Ebner, J. R., and Franchetti, V. M., *Chem. Rev.* **88**, 55 (1988).
35. Volta, J.-C., Bere, K., Zhang, Y. J., and Olier, R., ACS Symposium Series, Vol. **523**, p. 217 (S. T. Oyama and J. W. Hightower, Eds.), Am. Chem. Soc., Washington, DC, 1993.
36. Gai, P. L., and Kourtakis, K., *Science* **267**, 661 (1995).
37. Benabdelouahab, F., Ph.D. thesis L'ecole Centrale de Lyon, 1994.